IEEE Access
Multidisciplinary ⋮ Rapid Review ⋮ Open Access Journal

Received 10 April 2024, accepted 14 May 2024, date of publication 22 May 2024, date of current version 3 June 2024.

Digital Object Identifier 10.1109/ACCESS.2024.3404040

RESEARCH ARTICLE

Sensorless Control of Induction Motor Based on Super-Twisting Sliding Mode Observer With Speed Convergence Improvement

LELISA WOGI, MARCIN MORAWIEC, (Senior Member, IEEE), AND TADELE AYANA
Faculty of Electrical and Control Engineering, Gdańsk University of Technology, 80-233 Gdańsk, Poland
Corresponding author: Lelisa Wogi (lelisa.wogi@pg.edu.pl)

ABSTRACT The super twisting sliding-mode observer (ST-SMO) has been proposed to achieve an effective method for alleviating low-order harmonics of measured quantities, issues related to DC drift, and suppression of chattering due to low-frequency sampling. The conventional ST-SMO, on the other hand, suffers from control delay in the convergence trajectory due to the system disturbance, resulting in decreased anti-disturbance capability and impacting the estimation accuracy and energy consumption. This paper proposed an ST-SMO with convergence improvement to address the issue related to the sliding mode controller along the sliding surface. A nonlinear sliding mode manifold is created to achieve the optimal ST-SMO convergence trajectory along the sliding surface. Then, a disturbance compensation term is added to the control law to eliminate the system control delay. In comparison to the conventional ST-SMO, the investigated method can effectively improve the anti-disturbance capability of the induction motor (IM) Observer, resulting in improved speed estimation (rotor flux control under applied load torque disturbances, speed reversal, and zero speed operation), good performance, and stability. The simulation and experimental studies are carried out for an induction motor with a 5.5kW rating. Both simulation and experimental results prove good robustness against the applied load torque disturbances and convergence of rotor speed to its actual value.

INDEX TERMS Disturbance, stability analysis, sliding mode observer, super twisting.

NOMENCLATURE

"^ "	estimated values.
"∼"	Error of estimated values.
R_r, R_s	Rotor and stator resistance.
L_m	Main inductance.
$L_{s,r}$	Stator and rotor inductances.
T_L, T_e	Load, and electromagnetic torque.
J, B	Moment of inertia and friction coefficient.
$i_{s\alpha,\beta}$	Stator current vector components.
$V_{s\alpha,\beta}$	Stator voltage vector components.
$\psi_{r\alpha,\beta}$	Rotor flux vectors.
p.u	Per unit.
ω_r	Rotor angular speed.

The associate editor coordinating the review of this manuscript and approving it for publication was Qinfen Lu.

I. INTRODUCTION

Due to its improved speed-regulation performance, direct stator field-oriented control-based induction motor drives have been used in numerous industrial applications [1], [2]. Such practical applications include aviation control systems, locomotive traction systems, and electric vehicle drives, which require high system performance under severe and tough circumstances. The direct stator field-oriented control speed loop typically uses a closed-loop control structure.

The PI controller is the most frequently employed approach for the IM speed loop [3]. Static-errorless control can be achieved using linear control theory and pole-zero cancellation [4]. However, a precise IM model is necessary for pole-zero cancellation. The motor's precise practical applications will invariably be impacted by disturbances brought on by the ambiguity of motor parameters [5]. It also considers

fluctuations in motor resistance and inductance brought on by field saturation and temperature. As a result, the PI controller finds it challenging to achieve significant resilience of the IM speed loop. The other factor is the outside disturbance brought on by the speed loop output change [6]. It considers changes in load torque and the state of the motor. The speed loop degrades if the ability to reject the external disturbance is insufficient, preventing the actual speed from tracking its reference rapidly. Therefore, the existing loop's anti-disturbance capacity needs to be improved.

The Sliding Mode Control Observer (SMO) has been deemed an efficient method for enhancing the resilience of the speed observer [7], [8], [9]. However, the high-frequency switching control has led to a chattering issue. As a result, it has emerged as a key area for SMO enhancement through chattering suppression. First, approaches based on boundary layers have been presented for the Integral SMO [10], [11]. However, they mostly weaken the system's robustness to silence the noise. Additionally, the steady-state error problem with system disturbance exists [12].

A second-order sliding mode observer(SMO) based on the field-oriented control of SMC was proposed in [8]. Theoretically, putting the high-frequency switching control in its derivatives can eliminate chattering. In the meantime, the sliding-mode state and its first derivative are made to equal zero in a limited time [13] to solve the steady-state error problem. The super twisting high order was used to estimate the rotor position speed and mechanical speed, track the parameter variations with an online method, and is a tool for chattering attenuation [14], [15], [16], [17].

The primary benefit of the super-twisting observer is that it reduces chattering attenuation. The major advantage of utilizing speed observer is to lessen dependence on the estimated states and, thus, to spend less time processing data [18]. The results under a varying load torque demonstrate the convergence of the controlled states to the target value in a finite time with reduced chattering as the key characteristics of this combination. The adaptive SMO has been proposed to increase the robustness of motor drives [19], [20], [21], [22], [23]. The super twisting SMO (ST-SMO), a common Second Order SMO, is simple to design and well-suited for the first-order system [24], [25], [26]. The ST-SMO is used [16] to drive AC motor direct torque control (DTC), which can increase characteristic robustness to speed and torque transients.

To improve the performance of the suggested observer under an external disturbance, namely, the machine load torque, an observer based on the super-twisting theory [27] has been developed to estimate the rotor flux and rotor speed. It has been noted in [28] and [29], that while the ST-SMO can improve system static performance, it cannot account for small perturbations that increase over time or state variables. As a result, ST-SMO anti-disturbance capabilities still have a long way to go. The disturbance boundary of the IM speed observer is challenging to estimate or calculate, but the variable gains are developed based on two well-known functions of the disturbance boundary. A smoothing factor is added to the ST-SMO control law to lessen chattering when measurement noise is present [30]. The alteration does not, however, enhance the ability to compensate for disturbances.

The sliding surface is directed to zero by ST-SMO using a continuity function in the feedback, which lessens chattering. The difficulties of DC drift and lower-order harmonics present in the measured quantities are reduced when the mixed second and third-order generalized integrator is used, followed by the ST-SMO, as opposed to a pure integrator [31]. Moreover, it reduces chattering because ST-SMO operates at a low sampling frequency [32]. The alteration does not, however, enhance the ability to compensate for disturbances. To account for the system disturbance, the ST-SMO is combined with an additional controller which suppresses matched and mismatched disturbances [33], [34]. This paper proposed a convergence enhancement method for ST-SMO based on multiscalar control of IM observers to enhance the anti-disturbance performance of ST-SMO.

The optimal convergence improvement of ST-SMO is used to introduce a nonlinear sliding-mode manifold. In the case of the conventional ST-SMO, the disturbance will lead the system to diverge from the desired convergence, causing convergence delay and poor transient performance. A disturbance compensation term is developed and added to the conventional control rule based on the proposed sliding-mode manifold. Then, by forcing the system to converge along the ideal trajectory despite system disruption. It can offer satisfactory transient performance for precise practical applications in challenging working environments.

II. INDUCTION MOTOR MODEL

The mathematical model of an IM is represented in the (α-β) reference frame as in [32]:

$$\frac{di_{sa}}{dt} = -\frac{(R_sL_r^2 + R_rL_m^2)}{L_r w_\sigma} i_{sa} + \frac{R_rL_m}{L_r w_\sigma}\psi_{r\alpha} + \frac{L_m}{w_\sigma}\omega_r\psi_{r\beta} + \frac{L_r}{w_\sigma}V_{s\alpha} \quad (1)$$

$$\frac{di_{s\beta}}{dt} = -\frac{(R_sL_r^2 + R_rL_m^2)}{L_r w_\sigma} i_{s\beta} + \frac{R_rL_m}{L_r w_\sigma}\psi_{r\beta} - \frac{L_m}{w_\sigma}\omega_r\psi_{r\alpha} + \frac{L_r}{w_\sigma}V_{s\beta} \quad (2)$$

$$\frac{d\psi_{r\alpha}}{dt} = -\frac{R_r}{L_r}\psi_{r\alpha} - \omega_r\psi_{r\beta} + \frac{R_rL_m}{L_r} i_{sa} \quad (3)$$

$$\frac{d\psi_{r\beta}}{dt} = -\frac{R_r}{L_r}\psi_{r\beta} + \omega_r\psi_{ra} + \frac{R_rL_m}{L_r} i_{s\beta} \quad (4)$$

$$\frac{d\omega_r}{dt} = \frac{L_m}{JL_r}(\psi_{ra}i_{s\beta} - \psi_{r\beta}i_{sa}) - \frac{B}{J}\omega_r - \frac{T_L}{J} \quad (5)$$

where the designation of coefficient has been introduced as $w_\sigma = L_rL_s - L_m^2$

$$a_1 = -\frac{(R_sL_r^2 + R_rL_m^2)}{L_r w_\sigma}, a_2 = \frac{R_rL_m}{L_r w_\sigma}, a_3 = \frac{L_m}{w_\sigma}, a_4 = \frac{L_r}{w_\sigma},$$
$$a_5 = -\frac{R_r}{L_r}, a_6 = \frac{R_rL_m}{L_r}$$

III. PROPOSED CONTROL SYSTEM

The block diagram of the suggested ST-SMO for the speed observer based on multiscalar control is shown in Fig. 1. The entire system consists of an IM, a voltage source inverter, an observer, and a control unit. The reference speed (x_{11}^*) and rotor flux (x_{21}^*) serve as its inputs and the command electromagnetic and reactive torque serve as its output. Based on the applied reference flux linkage (x_{21}^*) and the reference speed (x_{11}^*), the proposed strategy block diagram is shown in Fig. 1. Conversely, electromagnetic reference torque (x_{12}^*) is produced from the PI speed control loop's output where the input to the PI speed controller is the error of reference speed and estimated speed ($e_{x_{11}}$). The inputs to the corresponding PI controllers that produce the control variables m_1 and m_2 are the errors between electromagnetic reference torque (x_{12}^*) and estimated electromagnetic torque ($\hat{x}_{12}$) and the error between reactive reference torque (x_{22}^*) and estimated reactive torque ($\hat{x}_{22}$) respectively. The nonlinearity compensation is done by creating control variables (u_1 and u_2) found in the multiscalar model from x_{12} and x_{22} by decoupling the system. These control variables will later transformed into the stator voltage $u_{s\alpha}$ and $u_{s\beta}$ components. Due to the multiscalar control decoupling ability over the other model, without reducing control performance, it is unaffected by the position of the stator current and flux vectors and does not require coordinate transformation. The only transformation stated in pink in the block diagram is the one given by (45). To create the gating signals (S_a, S_b and S_c), for the voltage source inverter (VSI) that provides the necessary voltage to operate the IM, the signals $u_{s\alpha}$ and $u_{s\beta}$ are eventually sent to the PWM block. The proposed ST-SMO estimates the speed of the induction motor. Its structure is presented in Fig. 2.

The differences between the modified ST-SMO and the standard ST-SMO are in the nonlinear sliding surface manifold modification to obtain a sliding surface equal to zero, that the system will be forced to follow the ST-ideal SMO provided the control law is tailored to ensure that the nonlinear sliding mode manifold slides along the sliding surface making it zero and modification of control law that the additional control term added. The primary strategy for solving these issues is enhanced anti-disturbance capabilities. To increase anti-disturbance performance from the standpoint of

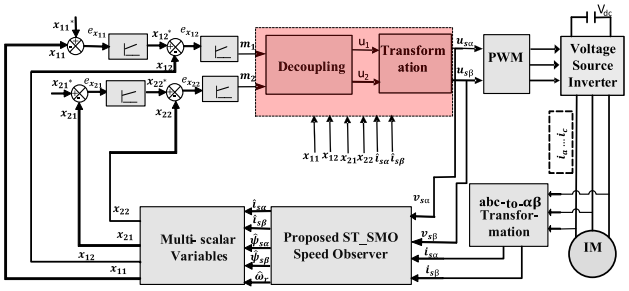

FIGURE 1. Block diagram of sensorless speed control of IM drives with the proposed ST-SMO-based speed observer.

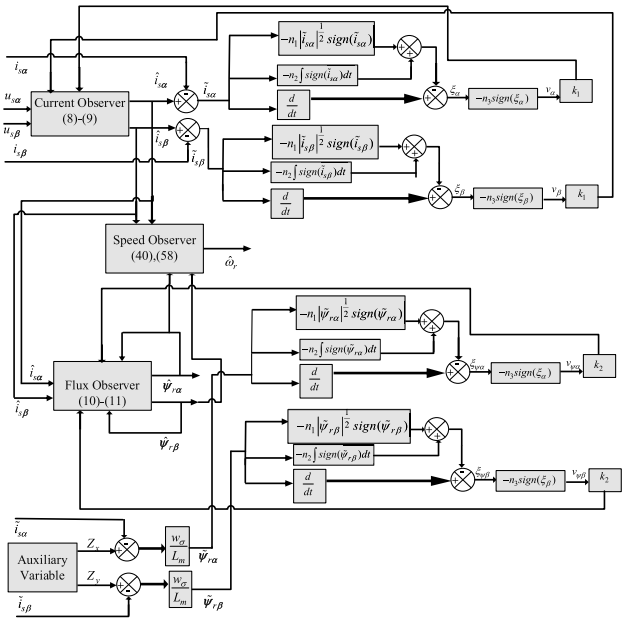

FIGURE 2. Schematic diagram of proposed ST-SMO speed observer.

convergence trajectory optimization, this research suggests an ST-SMO. Thus, the primary concept of the proposed ST-SMO is that the new sliding-mode manifold is introduced to the conventional ST-SMO, the additional control term is created and immediately included in the conventional control law based on the manifold modification, and under system disruption, the extra control term will compel the system to converge along the sliding surface, eliminating the delay.

First, to design an observer structure taking an assumption that the following flux observer is accessible.

$$\frac{d\hat{\psi}_{r\alpha}}{dt} = X_\alpha \tag{6}$$

$$\frac{d\hat{\psi}_{r\beta}}{dt} = X_\beta \tag{7}$$

where X_α and X_β are designed control law.

The super twisting sliding mode current and flux observer is designed as:

$$\frac{d\hat{i}_{sa}}{dt} = -a_4 R_s \hat{i}_{sa} - a_3 \frac{d\hat{\psi}_{r\alpha}}{dt} + a_4 V_{s\alpha} + v_\alpha \tag{8}$$

$$\frac{d\hat{i}_{s\beta}}{dt} = -a_4 R_s \hat{i}_{s\beta} - a_3 \frac{d\hat{\psi}_{r\beta}}{dt} + a_4 V_{s\beta} + v_\beta \tag{9}$$

$$\frac{d\hat{\psi}_{r\alpha}}{dt} = X_\alpha + v_{\psi\alpha} \tag{10}$$

$$\frac{d\hat{\psi}_{r\beta}}{dt} = X_\beta + v_{\psi\beta} \tag{11}$$

where the designations of coefficients have been introduced as

$$v_a = n_1 \left|\tilde{i}_{sa}\right|^{\frac{1}{2}} sign(\tilde{i}_{sa}) + n_2 \int sign(\tilde{i}_{sa})dt + V_1 \tag{12}$$

$$v_\beta = n_1 \left|\tilde{i}_{s\beta}\right|^{\frac{1}{2}} sign(\tilde{i}_{s\beta}) + n_2 \int sign(\tilde{i}_{s\beta})dt + V_2 \quad (13)$$

$$v_{\psi a} = n_4 sign(\tilde{\psi}_{ra}) + n_5 \int sign(\tilde{\psi}_{ra})dt + V_3 \quad (14)$$

$$v_{\psi\beta} = n_4 \left|\tilde{\psi}_{r\beta}\right|^{\frac{1}{2}} sign(\tilde{\psi}_{r\beta}) + n_5 \int sign(\tilde{\psi}_{r\beta})dt + V_4 \quad (15)$$

where the derivatives of the additional terms are;

$$\dot{V}_1 = -n_3 sign(\xi_\alpha) \quad (16)$$

$$\dot{V}_2 = -n_3 sign(\xi_\beta) \quad (17)$$

$$\dot{V}_3 = -n_6 sign(\xi_{\psi_{r\alpha}}) \quad (18)$$

$$\dot{V}_4 = -n_6 sign(\xi_{\psi_{r\beta}}) \quad (19)$$

also, the following terms in (16) - (19) are derived as in (20)- (23) respectively;

$$\xi_\alpha = \tilde{i}_{sa} + n_1 \left|\tilde{i}_{sa}\right|^{\frac{1}{2}} sign(\tilde{i}_{sa}) + n_2 \int sign(\tilde{i}_{sa})dt \quad (20)$$

$$\xi_\beta = \tilde{i}_{s\beta} + n_1 \left|\tilde{i}_{s\beta}\right|^{\frac{1}{2}} sign(\tilde{i}_{s\beta}) + n_2 \int sign(\tilde{i}_{s\beta})dt \quad (21)$$

$$\xi_{\psi_{r\alpha}} = \tilde{\psi}_{ra} + n_4 \left|\tilde{\psi}_{ra}\right|^{\frac{1}{2}} sign(\tilde{\psi}_{ra}) + n_5 \int sign(\tilde{\psi}_{ra})dt \quad (22)$$

$$\xi_{\psi_{r\beta}} = \tilde{\psi}_{r\beta} + n_4 \left|\tilde{\psi}_{r\beta}\right|^{\frac{1}{2}} sign(\tilde{\psi}_{r\beta}) + n_5 \int sign(\tilde{\psi}_{r\beta})dt \quad (23)$$

where $n_1, n_2 \ldots n_6$ are control signals, ξ_α, ξ_β, $\xi_{\psi_{r\alpha}}$, and $\xi_{\psi_{r\beta}}$ are nonlinear sliding-mode manifold surfaces.

The errors are defined as $\tilde{i}_{sa} = \hat{i}_{sa} - i_{sa}$, $\tilde{i}_{s\beta} = \hat{i}_{s\beta} - i_{s\beta}$,

$$\tilde{\psi}_{ra} = \hat{\psi}_{ra} - \psi_{ra}, \tilde{\psi}_{r\beta} = \hat{\psi}_{r\beta} - \psi_{r\beta}$$

In the conventional speed estimation technique, it is assumed that the real rotor flux is equal to the estimated rotor flux, and the estimated rotor flux error is ignored because the real rotor flux cannot be measured. The estimated rotor flux inaccuracy significantly impacts the stability and robustness of speed estimation. This study introduces the estimated rotor flux error to the speed estimation technique. The estimated rotor flux error should be improved because the error cannot be measured in industrial situations.

Now, the auxiliary quantities are introduced to find the rotor flux error as follows:

$$Z_x = \tilde{i}_{sa} + \frac{L_m}{w_\sigma}\tilde{\psi}_{ra} \quad (24)$$

$$Z_y = \tilde{i}_{s\beta} + \frac{L_m}{w_\sigma}\tilde{\psi}_{r\beta} \quad (25)$$

After differentiating (24) and (25), and simplification, the following is obtained.

$$\frac{dZ_x}{dt} = \frac{d\tilde{i}_{sa}}{dt} + \frac{L_m}{w_\sigma}\frac{d\tilde{\psi}_{ra}}{dt} = k_1 v_a \quad (26)$$

$$\frac{dZ_y}{dt} = \frac{d\tilde{i}_{s\beta}}{dt} + \frac{L_m}{w_\sigma}\frac{d\tilde{\psi}_{r\beta}}{dt} = k_1 v_\beta \quad (27)$$

From (24) and (25), rotor flux error is constructed from Z_x and Z_y as follows:

$$\tilde{\psi}_{ra} = \frac{w_\sigma}{L_m}(Z_x - \tilde{i}_{sa}) \quad (28)$$

$$\tilde{\psi}_{r\beta} = \frac{w_\sigma}{L_m}(Z_y - \tilde{i}_{s\beta}) \quad (29)$$

Using $\tilde{\psi}_{ra}$ and $\tilde{\psi}_{r\beta}$ variables, it is possible to add feedback gain of rotor flux error to the flux observer. Defining the current error as a model of estimation errors (8)– (9) has the following form:

$$\frac{d\tilde{i}_{sa}}{dt} = a_1\tilde{i}_{sa} + a_2\tilde{\psi}_{ra} + a_3\left(\tilde{\omega}_r\hat{\psi}_{r\beta} + \hat{\omega}_r\tilde{\psi}_{r\beta} - \tilde{\omega}_r\tilde{\psi}_{r\beta}\right) + k_1 v_a \quad (30)$$

$$\frac{d\tilde{i}_{s\beta}}{dt} = a_1\tilde{i}_{s\beta} + a_2\tilde{\psi}_{r\beta} - a_3\left(\tilde{\omega}_r\hat{\psi}_{ra} + \hat{\omega}_r\tilde{\psi}_{ra} - \tilde{\omega}_r\tilde{\psi}_{ra}\right) + k_1 v_\beta \quad (31)$$

It is possible to define functions X_α and X_β depending on the knowledge of estimated rotor fluxes ($\hat{\psi}_{ra}$ and $\hat{\psi}_{r\beta}$) and rotor flux errors ($\tilde{\psi}_{ra}$ and $\tilde{\psi}_{r\beta}$) variables for defining the flux observer as follows:

$$\frac{d\hat{\psi}_{r\alpha}}{dt} = X_\alpha = a_5\hat{\psi}_{r\alpha} - \hat{\omega}_r\hat{\psi}_{r\beta} + a_6\hat{i}_{sa} + k_2 v_{\psi\alpha} \quad (32)$$

$$\frac{d\hat{\psi}_{r\beta}}{dt} = X_\beta = a_5\hat{\psi}_{r\beta} + \omega_r\hat{\psi}_{ra} + a_6\hat{i}_{s\beta} + k_2 v_{\psi\beta} \quad (33)$$

Depending on (32) and (33), the dynamics of flux estimation errors are given as follows:

$$\frac{d\tilde{\psi}_{ra}}{dt} = a_5\tilde{\psi}_{ra} - \tilde{\omega}_r\hat{\psi}_{r\beta} - \hat{\omega}_r\tilde{\psi}_{r\beta} + \tilde{\omega}_r\tilde{\psi}_{r\beta} + a_6\tilde{i}_{sa} + k_2 v_{\psi a} \quad (34)$$

$$\frac{d\tilde{\psi}_{r\beta}}{dt} = a_5\tilde{\psi}_{r\beta} + \tilde{\omega}_r\hat{\psi}_{ra} + \hat{\omega}_r\tilde{\psi}_{ra} - \tilde{\omega}_r\tilde{\psi}_{ra} + a_6\tilde{i}_{s\beta} + k_2 v_{\psi\beta} \quad (35)$$

The observer structure (8) - (11) is unstable when stabilizing functions ($v_\alpha, v_\beta, v_{\psi\alpha}, v_{\psi\beta}$) are equal to zero because some observer poles have positive values. The following Lyapunov function can be selected to develop speed estimation, and the proposed observer structure must be asymptotically stable.

$$V_1 = \frac{1}{2}(\tilde{i}_{s\alpha}^2 + \tilde{i}_{s\beta}^2 + \tilde{\psi}_{r\alpha}^2 + \tilde{\psi}_{r\beta}^2) + \frac{1}{2}\frac{1}{\gamma_\omega}\tilde{\omega}_r^2 \quad (36)$$

and $\dot{V}_1$ is negatively determined as

$$\dot{V}_1 = \tilde{i}_{s\alpha}\dot{\tilde{i}}_{s\alpha} + \tilde{i}_{s\beta}\dot{\tilde{i}}_{s\beta} + \tilde{\psi}_{ra}\dot{\tilde{\psi}}_{ra} + \tilde{\psi}_{r\beta}\dot{\tilde{\psi}}_{r\beta} + \frac{1}{\gamma_\omega}\tilde{\omega}_r\dot{\tilde{\omega}}_r \leq 0 \quad (37)$$

The observer structure is asymptotically stable when the Lyapunov theorem is met. By developing calculations, it is possible to prove that to guarantee $\dot{V}_1 \leq 0$ as follows:

$$\dot{V}_1 = \begin{pmatrix} a_1\left(\tilde{i}_{s\alpha}^2 + \tilde{i}_{s\beta}^2\right) + a_5\left(\tilde{\psi}_{r\alpha}^2 + \tilde{\psi}_{r\beta}^2\right) + \\ \tilde{\omega}_r\left(\frac{1}{\gamma_\omega}\dot{\tilde{\omega}}_r + a_3\left(\hat{\psi}_{r\beta}\tilde{i}_{s\alpha} - \hat{\psi}_{ra}\tilde{i}_{s\beta}\right)\right) \\ + \left(\hat{\psi}_{ra}\tilde{\psi}_{r\beta} - \hat{\psi}_{r\beta}\tilde{\psi}_{ra}\right) \end{pmatrix} \leq 0 \quad (38)$$

where γ_ω should be greater than zero and is a gain.

The conventional rotor speed estimation ignoring rotor flux error is found from (38) as:

$$\dot{\hat{\omega}}_r = \gamma_\omega a_3 \left(\hat{\psi}_{r\alpha}\tilde{i}_{s\beta} - \hat{\psi}_{r\beta}\tilde{i}_{s\alpha}\right) \tag{39}$$

Using an adaptive system, it is possible to reproduce the rotor speed from (38) with rotor flux error as:

$$\dot{\hat{\omega}}_r = \gamma_\omega a_3 \left(\hat{\psi}_{r\alpha}\tilde{i}_{s\beta} - \hat{\psi}_{r\beta}\tilde{i}_{s\alpha}\right) + \left(\hat{\psi}_{r\beta}\tilde{\psi}_{r\alpha} - \hat{\psi}_{r\alpha}\tilde{\psi}_{r\beta}\right) \tag{40}$$

where γ_ω is a gain.

Stator currents errors are convergent in finite time, while the convergence of the speed and flux errors occurs asymptotically.

A. MULTISCALAR CONTROL VARIABLES

In the multiscalar control approach, the speed (x_{11}), torque (x_{12}), rotor flux modulus (x_{21}), and reactive torque (x_{22}) are used as state variables. The outer loop of the independent flux closed loop is subjected to negative feedback control to improve control resilience and accuracy in the face of parameter changes. The proposed technique, seen in Fig. 1, includes a speed and flux outer loop controller, and torque (x_{12} and x_{22}) computations. This approach uses four state variables based on rotor flux and stator current to the IM model given in [36], [37], and [38]. The multiscalar control of the IM is generated utilizing the following state variables.

$$\begin{aligned} x_{11} &= \hat{\omega}_r \quad x_{21} = \hat{\psi}_{r\alpha}^2 + \hat{\psi}_{r\beta}^2 \\ x_{12} &= \hat{\psi}_{r\alpha}\hat{i}_{s\beta} - \hat{\psi}_{r\beta}\hat{i}_{s\alpha} \quad x_{22} = \hat{\psi}_{r\alpha}\hat{i}_{s\alpha} + \hat{\psi}_{r\beta}\hat{i}_{s\beta} \end{aligned} \tag{41}$$

The torque x_{12}, is the vector product of the rotor flux and stator current vectors, whereas the reactive torque x_{22}, is the dot product of the same vectors. The multiscalar control method proposes a fourth-order model that properly captures the dynamic and static properties of the IM using the rotor flux and stator current state variables. Taking the derivatives of the variables specified in (41) yields:

$$\begin{aligned} \frac{d}{dt}x_{11} &= \frac{d}{dt}\hat{\omega}_r \\ \frac{d}{dt}x_{12} &= \hat{i}_{s\beta}\frac{d}{dt}\hat{\psi}_{r\alpha} + \hat{\psi}_{r\alpha}\frac{d}{dt}\hat{i}_{s\beta} - \hat{i}_{s\alpha}\frac{d}{dt}\hat{\psi}_{r\beta} - \hat{\psi}_{r\beta}\frac{d}{dt}\hat{i}_{s\alpha} \\ \frac{d}{dt}x_{21} &= 2\hat{\psi}_{r\alpha}\frac{d}{dt}\hat{\psi}_{r\alpha} + 2\hat{\psi}_{r\beta}\frac{d}{dt}\hat{\psi}_{r\beta} \\ \frac{d}{dt}x_{22} &= \hat{i}_{s\alpha}\frac{d}{dt}\hat{\psi}_{r\alpha} + \hat{\psi}_{r\alpha}\frac{d}{dt}\hat{i}_{s\alpha} + \hat{i}_{s\beta}\frac{d}{dt}\hat{\psi}_{r\beta} + \hat{\psi}_{r\beta}\frac{d}{dt}\hat{i}_{s\beta} \end{aligned} \tag{42}$$

After substitution and simplification, the following is obtained.

$$\begin{aligned} \frac{d}{dt}x_{11} &= \frac{L_m}{JL_r}x_{12} - \frac{T_L}{J}, \frac{d}{dt}x_{21} = \frac{-2}{T_r}(x_{21} - L_m x_{22}) \\ \frac{d}{dt}x_{12} &= -\tau_m x_{12} + m_1, \frac{d}{dt}x_{22} = -\tau_m x_{22} + m_2 \end{aligned} \tag{43}$$

where $\tau_m = \frac{L_s R_r - L_r R_s}{w_\sigma}$ is the electromagnetic time constant of the motor, T_r is the rotor time constant, J is a moment of inertia, T_L is load torque, m_1 and m_2 are the output of PI controllers used as control variables.

The nonlinearity compensation is done by creating control variables (u_1 and u_2) that are found in the multiscalar model from x_{12} and x_{22} (according to Fig. 1):

$$\begin{aligned} u_1 &= \frac{w_\sigma}{L_r}(\tau_m m_1 + x_{11}x_{22} + \frac{L_m}{w_\sigma}x_{11}x_{21}) \\ u_2 &= \frac{w_\sigma}{L_r}(\tau_m m_2 - x_{11}x_{22} - \frac{R_r L_m}{L_r w_\sigma}x_{21} - \frac{R_r L_m}{L_r}(\frac{x_{12}^2 + x_{22}^2}{x_{21}})) \end{aligned} \tag{44}$$

These control variables will later transformed into the stator voltage components as follows:

$$u_{s\alpha} = \frac{u_2\hat{\psi}_{r\alpha} - u_1\hat{\psi}_{r\beta}}{x_{21}}, u_{s\beta} = \frac{u_1\hat{\psi}_{r\alpha} + u_2\hat{\psi}_{r\beta}}{x_{21}} \tag{45}$$

IV. STABILITY ANALYSIS

The adaptive observer in the $\alpha\beta$-reference frame exhibits more complicated nonlinear properties than other observers in the dq-reference frame. To simplify the analysis, the observer error system is characterized using the small signal linearization approach, and the steady state operating point is produced by linearizing the system in the dq-reference frame. The linearized system has a general form:

$$\frac{d}{dt}\Delta\mathbf{x}(t) = \mathbf{A}\Delta\mathbf{x}(t) + \mathbf{B}\Delta\mathbf{u}(t) \tag{46}$$

where $\mathbf{A}$ and $\mathbf{B}$ are the Jacobian matrices and $\Delta\mathbf{x}(t) = [\tilde{i}_{sd}, \tilde{i}_{sq}, \tilde{\psi}_{rd}, \tilde{\psi}_{rq}]^T$, $\Delta\mathbf{u}(t)$ is known as control inputs.

The estimator system is oriented with the rotor flux vector $\vec{\psi}_r$, so $\left|\vec{\psi}_r\right| = \sqrt{\psi_{rd}^{*2} + \psi_{rq}^{*2}}$ and the stator current vector components and ω_ψ can be treated as follows:

$$i_{sd} = \frac{\psi_{rd}^*}{L_m}, i_{sq} = \frac{T_L^*}{a_4\psi_{rd}^*} \tag{47}$$

Considering general form for $\Delta\mathbf{u}(t) = 0$, the linearized observer's errors model has the form

$$\Delta\dot{\mathbf{x}} = \mathbf{A}\Delta\mathbf{x} + \Delta\mathbf{A}\hat{\mathbf{x}}, \Delta\mathbf{i}_s = \mathbf{B}\Delta\mathbf{x} \tag{48}$$

where $\mathbf{x} = \left[\mathbf{i}_s\ \boldsymbol{\psi}_r\right]^\mathbf{T}$, $\mathbf{i}_s = \left[\mathbf{i}_{sd}\ \mathbf{i}_{sq}\right]^\mathbf{T}$, $\boldsymbol{\psi}_r = \left[\boldsymbol{\psi}_{rd}\ \boldsymbol{\psi}_{rq}\right]^\mathbf{T}$

$$\mathbf{A} = \begin{bmatrix} a_{11} & \omega_e & a_{12} & 0 \\ -\omega_e & -a_{11} & 0 & a_{12} \\ a_{13} & 0 & -a_{14} & \omega_{sl} \\ 0 & a_{13} & -\omega_{sl} & a_{14} \end{bmatrix},$$

$$\Delta\mathbf{A} = \begin{bmatrix} 0 & 0 & 0 & 0 \\ 0 & 0 & 0 & 0 \\ 0 & 0 & 0 & \Delta\omega_r \\ 0 & 0 & -\Delta\omega_r & 0 \end{bmatrix}$$

$$\mathbf{B}=\begin{bmatrix} B_{11} & 0 & -B_{12} & 0 \\ 0 & B_{11} & 0 & -B_{12} \end{bmatrix}, a_{11}=\frac{R_s L_r}{w_\sigma}, a_{12}=\frac{R_s L_m}{w_\sigma},$$
$$a_{13}=\frac{R_r L_m}{w_\sigma}, a_{14}=\frac{R_r L_s}{w_\sigma}, B_{11}=\frac{L_r}{w_\sigma}, B_{12}=\frac{L_m}{w_\sigma},$$

The solution of (48) is as follows:

$$\Delta\tilde{\mathbf{i}}_s=[s\mathbf{I}-\mathbf{A}]^{-1}\Delta\mathbf{A}\hat{\mathbf{x}} \tag{49}$$

where

$$[s\mathbf{I}-\mathbf{A}]^{-1}=\frac{1}{|s\mathbf{I}-\mathbf{A}|}\begin{bmatrix} b_{11} & b_{12} & b_{13} & b_{14} \\ b_{21} & b_{22} & b_{23} & b_{24} \\ b_{31} & b_{32} & b_{33} & b_{34} \\ b_{41} & b_{42} & b_{43} & b_{44} \end{bmatrix} \tag{50}$$

where the coefficients of the inverse matrix [s $\mathbf{I}-\mathbf{A}$] are represented by the terms b_{ij}. The open-loop transfer function for the speed error ($\Delta\omega_r$) is obtained as follows.

$$\frac{\Delta\omega_r}{\omega_r}=G_{Conv}(s)\hat{\psi}_r^2 \tag{51}$$

where $G_{Conv}(s)$ is conventional transfer function and given as;

$$G_{Conv}(s)=\frac{1}{|s\mathbf{I}-\mathbf{A}|}[B_{12}b_{33}-B_{11}b_{13}] \tag{52}$$

Substituting b_{13} and b_{33} in (52), where b_{13} and b_{33} are coefficients of the inverse matrix, an open loop transfer function is given as follows:

$$G_{Conv}(s)=\frac{1}{|s\mathbf{I}-\mathbf{A}|}\begin{bmatrix} s^3+(a_{11}+a_{14})s^2+\delta a_{11}a_{14}s+\omega_e^2 s \\ +(a_{11}\omega_e\omega_{sl}+a_{14}\omega_e^2) \end{bmatrix} \tag{53}$$

Hence, the transfer function has the form

$$\frac{\hat{\omega}_r}{\Delta\omega r}=(kp+\frac{ki}{s})G_{Conv}(s)\hat{\psi}_r^2 \tag{54}$$

where it is assumed that $k_p=0$ and $k_i=\gamma>0$.

The conventional and proposed speed estimation is discussed in this section to enhance the dynamic performance of speed estimation. The graphs were displayed to examine the dynamic performance of the system.

An efficient way to evaluate the stability and dynamic performance is to use the pole-zero map of an open-loop transfer function. To guarantee the stability of speed estimation, all of the poles and zeros have to remain in the left-hand plane. In (54) with rotor speed ranging from −1.0 to 1.0 p.u. the pole zero-map is shown in Fig. 3(a and b). The system is unstable

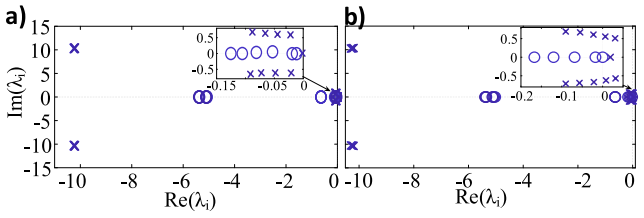

FIGURE 3. Pole-zero map of (54) with a conventional method a) rotor speed changing from 0.1 to 1 p.u. b) rotor speed changing from -0.5 to 1 p.u.

when some of the zeros are on the right-hand plane when the motor is at low speed or regenerating mode.

The relationship between the coefficient selection and system dynamic performance is examined in this section using the Bode diagram. The bode diagram of (54) with PI correction of $k_c=0$ is shown in Fig. 4(a and b), under rated load conditions. It is decided to use rotor speeds from −1 p.u to 1 p.u. The phase margin of the transfer function (54) must be within 90° to ensure system stability because the speed estimation of the AFO is built using the principle of Lyapunov stability. Fig. 4a shows that the AFO is stable without a load from 0.1 p.u to 1 p.u. in motoring mode. However, in Fig. 4b, the system is unstable because the maximum phase would exceed 90° when the speed dropped with the rated load and in regenerating mode. As a result, the AFO is unstable at ultralow speeds and regenerating mode under the rated load situation.

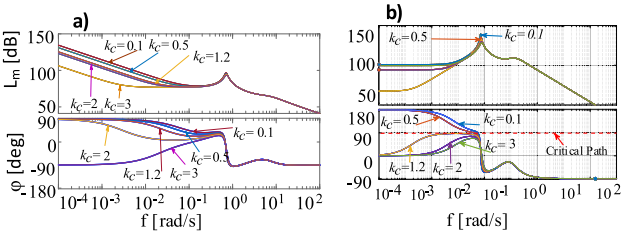

FIGURE 4. Bode diagram of (54) with conventional method under the rated load a) rotor speed changing from 0.1 to 1 p.u, b) rotor speed changing from −0.5 to 0.5 p.u.

V. PROPOSED ROTOR SPEED ESTIMATION

This sub-section considers the improved rotor speed estimation with a rotor flux error consideration.

The open-loop transfer function for the speed error can be obtained from the following.

$$\frac{\Delta\omega_{rN}}{\omega_r}=G_N(s)\hat{\psi}_r^2 \tag{55}$$

where $G_N(s)$ is the new transfer function and given as:

$$G_N(s)=\frac{1}{|s\mathbf{I}-\mathbf{A}|}\times\begin{bmatrix} B_{12}b_{33}-B_{11}b_{13}+k_f k_c(B_{12}b_{33}-B_{11}b_{13}) \\ +(B_{11}b_{14}-B_{12}b_{34}) \end{bmatrix} \tag{56}$$

k_c is a positive gain constant and $k_f=sign(\omega_r)$.

Hence, the transfer function has the form

$$\frac{\hat{\omega}_r}{\Delta\omega r}=(kp+\frac{ki}{s})G_N(s)\hat{\psi}_r^2 \tag{57}$$

In the conventional speed estimation shown in (39), the error signals use measured currents compared to the estimated currents, and then speed is estimated. To improve stability, the stabilizing function with rotor flux error is included in the speed estimation in the improved speed estimation. The speed adaptive law given in (39) is adjusted as in (40) to ensure the

stability of the speed adaptive error since the conventional speed estimation is unstable as stated in the previous section. The improved adaptive rotor speed estimation method is taken into consideration, and the modified speed adaptive equation is obtained by,

$$\dot{\hat{\omega}}_r = \gamma_\omega \left(\left(\hat{\psi}_{ra} \tilde{i}_{s\beta} - \hat{\psi}_{r\beta} \tilde{i}_{s\alpha} \right) + \left(\hat{\psi}_{r\beta} \tilde{\psi}_{ra} - \hat{\psi}_{ra} \tilde{\psi}_{r\beta} \right) + k_c k_f \hat{s}_\omega \right) \tag{58}$$

where $\hat{s}_\omega$ is a stabilizing function given in [35].

When the roots of (56) are solved using various k_c values, it can be seen in Fig. 5a that for lower k_c values, the real component of unstable zero is located on the imaginary axis of the s-plane in the regenerating mode. The system's stability improves as the value is increased starting from 0.1, as seen in Fig. 5(a and b) as the unstable zero shifts from the right to the left side of the s-plane. To guarantee that the real component of unstable zero resides in the left half of the s-plane for this article, the value should be greater than 0.5, with the range of 0.5 to 5 being considered. In a broader sense, the numerator coefficients can be solved to obtain the value of k_c, and a separate value is considered for determining the stable gain k_c. Then, through the estimation, the rotor speed varies from -1 to 1 rad/s (p.u). The minimal value of k_c has been determined to be positive and should be $k_c > 0.5$ for classical speed estimation. Still, in the case of an updated AFO, the system is stable even if k_c reaches zero.

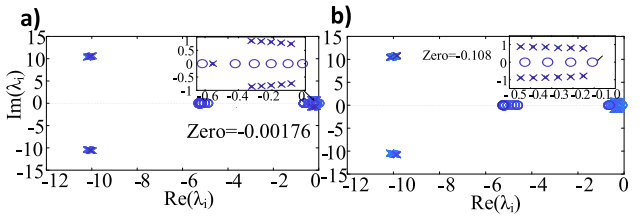

FIGURE 5. Pole-zero map of (53) with a conventional method rotor speed changing from a) -1 to 1 p.u, $k_c = 0.5 \ldots 3$, $\gamma_\omega = 0.5$, b) -1 to 1 p.u, $k_c = 2 \ldots 8$, $\gamma_\omega = 0.5$.

As can be observed, after applying the suggested stabilizing function and rotor flux error, the maximum phase is constrained to 90°, indicating that the system is now stable. The system is prone to instability as the maximum phase approaches 90°, in any case. As a result, the k_c choice should be a compromise between stability and dynamic performance improvement. This article proposes including the stabilizing function with rotor flux error instead of restricting the design to the single objective of stability, as used in feedback gain design. It also introduces a new term that permits the displacement of poles from unstable regions to stable ones for improving dynamic performance.

The Bode plot of a point operating below the lowest value of k_c with a speed of -1 to 1 (p.u) rad/s is shown in Fig. 6a. This system is unstable because the maximum phase would exceed 90° when the value of k_c is smaller. As a result, the system is unstable at a lower value of k_c. The bode plot of a point operating at the lowest value of k_c with a speed of -1 to 1 (p.u) rad/s is shown in Fig. 6b. This system is robustly stable since the gain margin is unlimited and the phase margin is positive.

It has been found that the system is stable with various k_c gains at different operating points. The work has centered on enhancing the improved speed estimation algorithms for stability improvement. Moreover, parameter uncertainties and nonlinearities at low speeds could lead to an incorrect speed estimation. The enhanced approach increases the accuracy of the speed estimation. In-depth simulations and tests are also used to study the system, and it is discovered to be stable under all feasible operating situations.

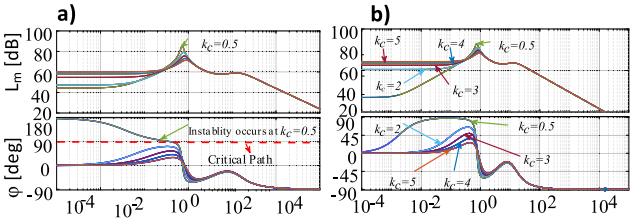

FIGURE 6. Bode diagram of the system under the rated load with rotor speed changing from -1 to 1 p.u, $k_c = 0.5 \ldots 5$, $\gamma_\omega = 1$, a) conventional method b) proposed method.

In Fig. 7 the pole-zero map and bode plot of updated law for both the motoring mode and regenerating mode operating point are displayed. The influence of changes value of kc from 0.1 to 3 is shown and visible in Fig. 7b that for k_c around zero, the proposed system (57) is stiff towards the critical path for the small speed value of rotor speed and regenerating mode. In contrast, the structure is still stable as shown in Fig.7(a and b).

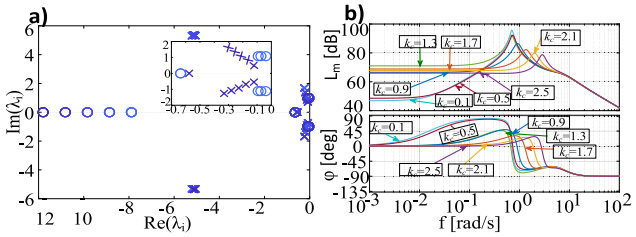

FIGURE 7. Pole zero map and Bode diagram of the proposed method under the rated load with rotor speed changing from -1 to 1 p.u, $k_c = 0.1 \ldots 3$, $\gamma_\omega = 0.5$.

VI. SIMULATION RESULTS

The simulations are done at various speed ranges when the motor is loaded. Figure 8a shows that the speed begins at 0.1 rad/s p.u and progressively increases and is maintained constant at 1 rad/s p.u. After 8s, the speed command is changed from 1 to -1 rad/s p.u. The simulation findings show that the proposed stabilizing function-based adaptation technique improves the drive operation stability. When defined stabilizing function-based adaptation is employed,

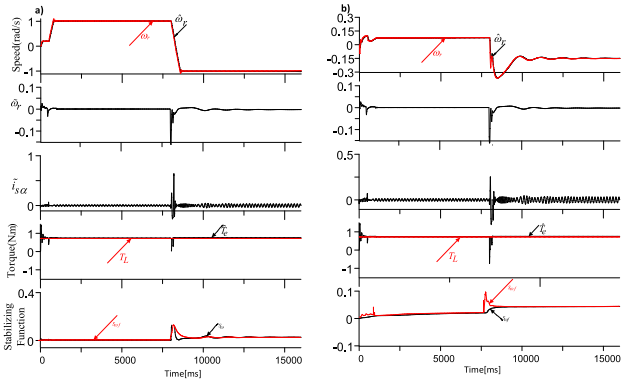

FIGURE 8. Simulation results of IM under the rated load with rotor speed a) changing from 1 to −1 p.u, b) changing from 0.1 to −0.1 p.u.

the speed error is too small as shown in Fig.8 (a and b). To test the proposed system for speed reversal, a step change of 0.1 rad/s p.u for 8 s before reversing to −0.1 rad/s p.u for 8 s is applied. Furthermore, the induction motor drives rated load torque is applied. During speed reversals, the speed goes through zero, causing the speed error to diverge. Using the proposed system reduces the instability problem as shown in Fig. 8b at low speed under the rated load. Under both motoring and regenerating modes, the ripples in speed and machine torque are negligible. The simulations revealed a considerable sensitivity to stator resistance fluctuations at low speeds under rated load.

VII. EXPERIMENTAL RESULTS

The specified experimental tests were conducted on the 5.5 kW, 400V/11A, 50Hz, 1420rpm driving system using a DC motor load as shown in Fig. 9. The control method was based on multi-scalar variables [36] and the proposed observer structures were integrated into the interface of a DSP Sharc ADSP21363 floating-point signal processor and an Altera Cyclone 2 FPGA. The transistor switching frequency was 3.3 kHz, and the sampling duration was 150 μS. Table 1 shows the nominal parameters for IM, Table 2 shows the adaptive PI gains of the system and Table 3 shows the gains of the observer.

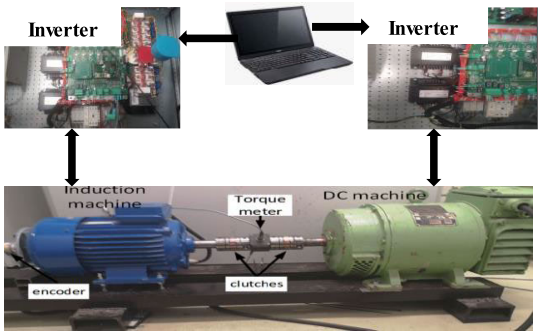

FIGURE 9. Experimental setup.

TABLE 1. IM parameters and references unit.

Symbol	Quantity	Values
R_s	stator resistance	2.92 Ω/0.035 p.u
R_r	rotor resistance	3.36 Ω/0.032 p.u
L_m	magnetizing inductance	0.422 H/1.95 p.u
L_s, L_r	stator and rotor inductance	0.439 H/2.04 p.u
L_σ	leakage inductance	0.017 H/0.09 p.u
P_n	nominal power	5.5 kW
I_n	nominal stator current (Y)	11 A
U_n	nominal stator voltage (Y)	400 V
n	nominal rotor speed	1420 rpm
f	nominal frequency	50 Hz
U_b=U_n	reference voltage	400 V
$I_b = I_n\sqrt{3}$	reference current	19 A
P_b	reference power	7.6 kW

TABLE 2. Adaptive PI gains of sensorless control system.

Name	k_p (p.u)	k_i (p.u)
$x_{11}(\omega_r)$	6	0.01 p.u
$x_{12}(T_e)$	5	0.028 p.u
$x_{21}(\hat{\psi}_r^2)$	10	0.01 p.u
$x_{22}(T_r)$	5	0.028 p.u

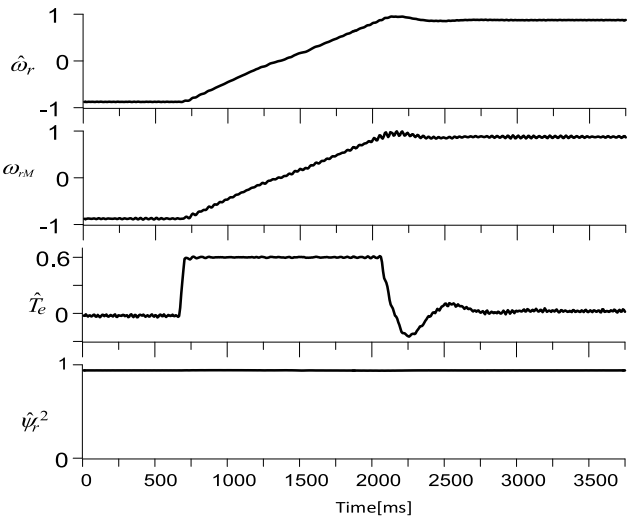

FIGURE 10. The experimental results during speed reversal from regenerating mode to motoring mode of operation.

A. MOTORING AND REGENERATING MODE OF OPERATION

Fig. 10 displays the experimental findings of testing the step speed change performance of the drive using a proposed system from regenerating to motoring mode of operation. The findings show a good speed tracking ability from −1 to 1 rad/s p.u. Fig. 11 shows experimental findings for the IM drives from motoring to regenerative mode of operation which occurs from the first quadrant to the second and fourth

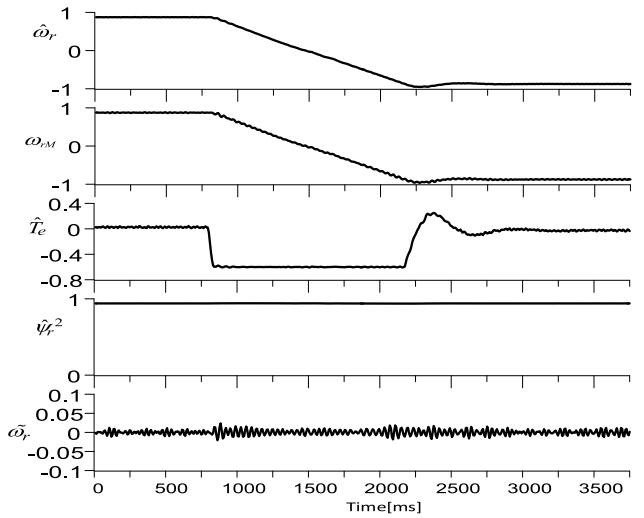

FIGURE 11. The experimental results during speed reversal motoring mode to regenerating mode of operation.

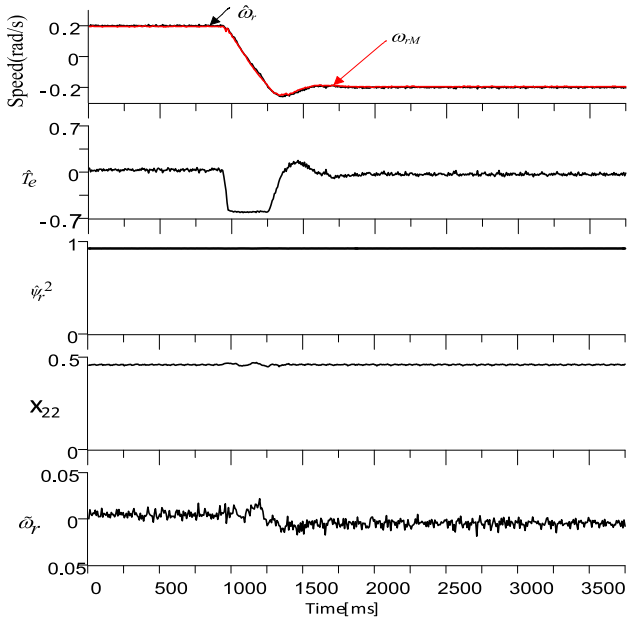

FIGURE 12. The experimental results in low-speed regeneration operation range of speed reversal test from +0.2 to −0.2 rad/s p.u.

quadrants. The result shows that the estimated speed follows the reference speed well, and the speed error is very small. The proposed approach for speed sensorless IM drives provides an accurate and stable estimate for wide-speed reversals in the motoring and regenerating mode of operations.

B. LOW-SPEED OPERATION PERFORMANCE

Fig. 12 shows the performance of the proposed speed estimation at low speeds. The estimated speed closely matches the reference speed at a low speed of 0.2 rad/s. The proposed approach provides a more accurate and stable estimation for low-speed reversals in the motoring and regenerating mode of

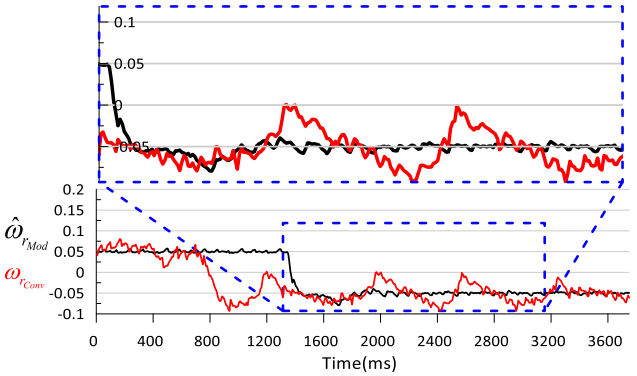

FIGURE 13. Experimental results in low-speed regeneration operation range of speed reversal test from +0.05 to −0.05 rad/s p.u. for conventional method (red (ω_{rConv})) vs Modified method (black($\hat{\omega}_{\mathrm{rConv}}$)).

TABLE 3. Gains of speed observer.

Name	Values (p.u)
k_c	0.1− 8
γ_ω	0.1− 1
k_1	0.3
k_2	0.05
n_1	0.2
n_2	0.1
n_3	0.05
n_4	0.1
n_5	0.05

operation. In Fig. 12, the estimated and real speed difference error is minimal. As shown in Fig. 13, the proposed observer's response at a very low speed, even at 0.05 rad/s, confirms that the proposed estimated rotor speed ($\hat{\omega}_{rConv}$) converges with the rotor speed and tracks the reference rotor speed with a very small inaccuracy over conventional ST-SMO (ω_{rConv}). The oscillations of the estimated speed are determined by the gains chosen values.

C. ZERO-SPEED OPERATION PERFORMANCE

Fig. 14 depicts the performance of the proposed system of speed sensorless IM drives during zero-speed operation. The speed step changes from 0.1 rad/s p.u. to zero. The studies revealing that the IM system successfully functioned at zero speed, as shown in Fig. 14, ensure the stability of the sensorless IM system in the ultra-low-speed zone.

Fig. 15 shows the performance of the proposed speed estimation at very low speeds of 0.015 rad/s p.u. with a load torque of −0.02Nm p.u. The estimated speed closely matches the reference speed even at a low speed of 0.015 rad/s with regenerative load torque. The proposed approach of speed sensorless control of IM drives provides a more accurate and stable estimation for low-speed reversals in the motoring and regenerating mode of operation.

TABLE 4. Comparison between classical and proposed approach.

Method	Speed Estimation with flux Error	Advantages	Disadvantages
[4]	No	Faster observer convergence	Estimated speed is unstable at low-speed regenerating mode
[12]	No	Wide-range speed estimation Stability is guaranteed	Large speed error due to parameter variation
[11]	No	Improved rotor speed estimation and its impact on sensorless control robustness, particularly near zero or zero rotor speeds.	Convergence of rotor flux depends on the Z surfaces and cannot be analyzed independently
Proposed	Yes	Ensures accurate speed estimation throughout all speed ranges, with less error due to parameter deviations and increased stability.	complex design procedure

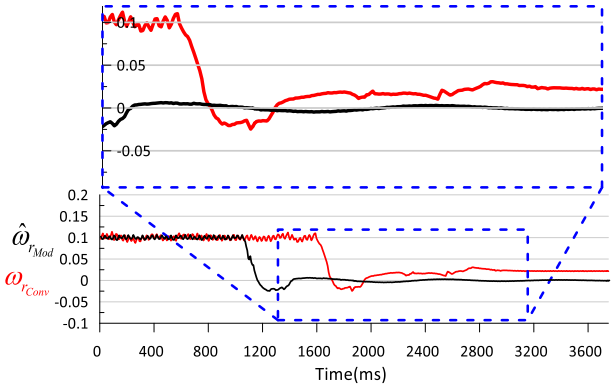

FIGURE 14. The experimental results at zero speed operation of the Conventional method (red(ω_{rConv})) with the modified method (black($\hat{\omega}_{rMod}$)).

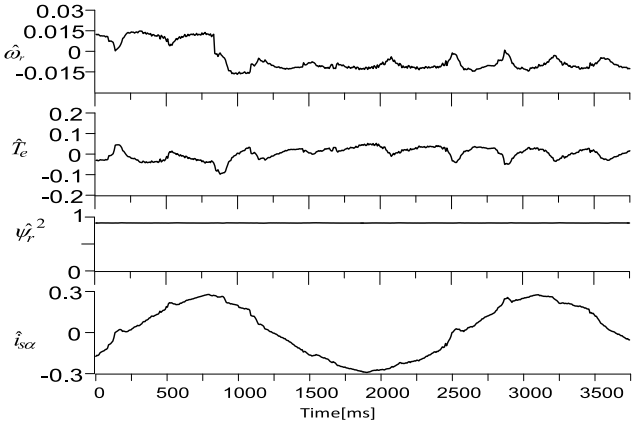

FIGURE 15. The experimental results of the proposed method under the load torque and ultralow speed operation.

D. LOAD TORQUE INJECTIONS

In Fig. 16, when the induction motor runs at a speed of 0.1 rad/s p.u, the load torque value is +0.7 Nm p.u. (motoring mode) is abruptly applied. Then after 0.5s, the load torque is changed to −0.7 Nm p.u. (regenerating mode). For this case, after 0.5s ($T_L \sim -0.7$ Nm p.u.), the conventional method is unstable, and after 1.5s machine is stopped. The findings show good speed tracking ability at 0.1rad/s p.u. stable with motoring mode but unstable at regenerating mode. In Fig. 17 the load torque value of the IM is changed from +0.7 Nm (motoring mode) to −0.7 Nm (regenerating mode). The AFO experiment results employ the proposed speed estimation approach, in which speed is evaluated using (58). For this case, after 1.5s ($T_L \sim -0.7$ Nm p.u.) the proposed method is stable for regenerating mode. The figure shows that the motor's speed oscillates somewhat, with a recovery

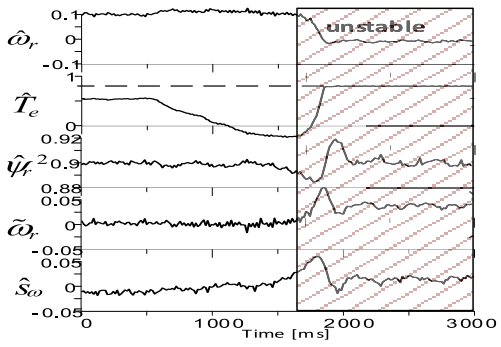

FIGURE 16. The load torque changes from motoring mode +0.7 Nm p.u to regenerating mode −0.7 Nm p.u for conventional method.

time of 1s. The control system recovers the oscillation. Even when load torque is applied suddenly, the estimated speed

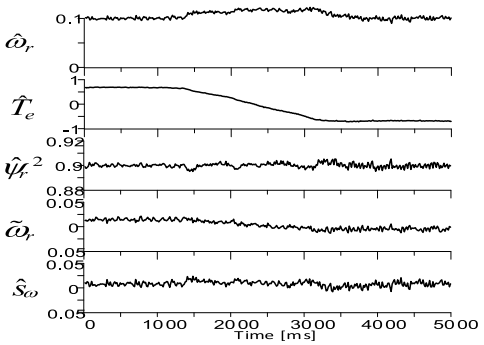

FIGURE 17. The load torque changes from motoring mode +0.7 Nm p.u to regenerating mode −0.7 Nm p.u for the proposed method.

remains consistent with the reference value. The error oscillates within ± 0.02 rad/s p.u due to load disturbances when load is applied, but soon some of the error is recovered and reduced to ± 0.009 rad/s p.u. The proposed system approach maintains the motor's inaccuracy even when a load is rapidly imposed, as seen in Fig. 17.

Table 4 compares existing approaches and suggested methods for ST-SMO. Existing approaches solely examine the design of feedback gains and employ conventional speed estimation, ignoring estimated rotor flux error. This will impact observer convergence, preventing the estimated rotor speed from converging to its true value, while the proposed approach improves the estimated rotor speed convergence to its true value.

VIII. CONCLUSION

The proposed Super Twisting SMO for high-performance sensorless speed control of IM was suggested in this work. The proposed approach incorporates a sliding-mode manifold by the ideal convergence of ST-SMO, which resolves the chattering issue and enhances the system's robustness and stability. The Lyapunov stability theorem has been used to mathematically examine and demonstrate the system's stability. The simulation results show how superior the proposed system is at rejecting disturbances, and load changes, and operating at a low-speed regenerating mode of operation. Additionally, the proposed ST-SMO produced superior outcomes when operated in a closed loop. It is evident from the experimental results of this study that the significant advancements are; that conventional ST-SMO innate chattering is eliminated, the rotor speed responds quickly in a transitory situation, and the proposed ST-SMO enables the system to be of extremely high precision and good track. Generally, the outcomes show that the approach devised in this study offers a very alluring and potential speed control for high-performance AC drives.

REFERENCES

[1] O. E. M. Youssef, M. G. Hussien, and A. E.-W. Hassan, "A new simplified sensorless direct stator field-oriented control of induction motor drives," *Frontiers Energy Res.*, vol. 10, pp. 1–8, Sep. 2022.

[2] L. Wogi, A. Thelkar, T. Tahiro, T. Ayana, S. Urooj, and S. Larguech, "Particle swarm optimization based optimal design of six-phase induction motor for electric propulsion of submarines," *Energies*, vol. 15, no. 9, p. 2994, Apr. 2022.

[3] J. P. Mishra, L. Wang, Y. Zhu, X. Yu, and M. Jalili, "Cascade PI-continuous second-order sliding mode control for induction motor," in *Proc. 43rd Annu. Conf. IEEE Ind. Electron. Soc.*, Beijing, China, Dec. 2017, pp. 6510–6515.

[4] Y. Wang, X. Deng, and C. Wu, "A new method for PI parameter adjustment of induction motor based on MRAS," in *Proc. IEEE 4th Adv. Inf. Technol., Electron. Autom. Control Conf. (IAEAC)*, Chengdu, China, Dec. 2019, pp. 500–504.

[5] B. Wang, Z. Dong, Y. Yu, G. Wang, and D. Xu, "Static-errorless deadbeat predictive current control using second-order sliding-mode disturbance observer for induction machine drives," *IEEE Trans. Power Electron.*, vol. 33, no. 3, pp. 2395–2403, Mar. 2018.

[6] A. V. R. Teja, C. Chakraborty, and B. C. Pal, "Disturbance rejection analysis and FPGA-based implementation of a second-order sliding mode controller fed induction motor drive," *IEEE Trans. Energy Convers.*, vol. 33, no. 3, pp. 1453–1462, Sep. 2018.

[7] X. Liu and H. Yu, "Continuous adaptive integral-type sliding mode control based on disturbance observer for PMSM drives," *Nonlinear Dyn.*, vol. 104, no. 2, pp. 1429–1441, Apr. 2021.

[8] W. Yu, S. D. Huang, and D. Jiang, "A fault monitoring method for wind power generation system based on sliding mode observer," *Arch. Electr. Eng.*, vol. 67, no. 3, pp. 625–643, Sep. 2020.

[9] S. Navaneethan, S. Kanthalakshmi, and S. A. Baggio, "Lyapunov stability based sliding mode observer for sensorless control of permanent magnet synchronous motor," *Bull. Polish Acad. Sci. Tech. Sci.*, vol. 70, Jan. 2022, Art. no. 140353.

[10] M. S. Mousavi, S. A. Davari, V. Nekoukar, C. Garcia, and J. Rodriguez, "Integral sliding mode observer-based ultralocal model for finite-set model predictive current control of induction motor," *IEEE J. Emerg. Sel. Topics Power Electron.*, vol. 10, no. 3, pp. 2912–2922, Jun. 2022.

[11] M. Morawiec and A. Lewicki, "Application of sliding switching functions in backstepping based speed observer of induction machine," *IEEE Trans. Ind. Electron.*, vol. 67, no. 7, pp. 5843–5853, Jul. 2020.

[12] R. Maamouri, M. Trabelsi, M. Boussak, and F. M'Sahli, "Second-order SMO-based sensorless control of IM drive: Experimental investigations of observer sensitivity and system reconfiguration in postfault operation mode," *IET Electric Power Appl.*, vol. 15, no. 7, pp. 811–823, Mar. 2021.

[13] G. Bartolini, E. Punta, and T. Zolezzi, "First and second order slide mode regularization techniques: The approximability property," *IFAC Proc. Volumes*, vol. 38, no. 1, pp. 878–882, 2005.

[14] S. Di Gennaro, J. Rivera Domínguez, and M. A. Meza, "Sensorless high order sliding mode control of induction motors with core loss," *IEEE Trans. Ind. Electron.*, vol. 61, no. 6, pp. 2678–2689, Jun. 2014.

[15] Y. Zhao, H. Yu, and S. Wang, "An improved super-twisting high-order sliding mode observer for sensorless control of permanent magnet synchronous motor," *Energies*, vol. 14, no. 19, p. 6047, Sep. 2021.

[16] M. Horch, A. Boumédiène, and L. Baghli, "Sensorless high-order super twisting sliding modes vector control for induction motor drives," in *Proc. 8th Int. Conf. Model., Identificat. Control (ICMIC)*, Nov. 2016, pp. 237–242.

[17] S. E. Farhi, D. Sakri, and N. Golea, "High-performance induction motor drive based on adaptive super-twisting sliding mode control approach," *Arch. Electr. Eng.*, vol. 71, no. 1, pp. 245–263, Mar. 2022.

[18] M. Morawiec, A. Lewicki, and F. Wilczynski, "Speed observer of induction machine based on backstepping and sliding mode for low-speed operation," *Asian J. Control*, vol. 23, no. 2, pp. 636–647, Jan. 2020.

[19] P. R. Kumar, A. K. Behera, and B. Bandyopadhyay, "Robust finite-time tracking of stewart platform: A super-twisting like observer-based forward kinematics solution," *IEEE Trans. Ind. Electron.*, vol. 64, no. 5, pp. 3776–3785, May 2017.

[20] I. Bakhti, S. Chaouch, and A. Maakouf, "High performance backstepping control of induction motor with adaptive sliding mode observer," *Arch. Control Sci.*, vol. 21, no. 3, pp. 331–344, Jan. 2011.

[21] S. El Daoudi, L. Lazrak, and M. Ait Lafkih, "Sliding mode approach applied to sensorless direct torque control of cage asynchronous motor via multi-level inverter," *Protection Control Modern Power Syst.*, vol. 5, no. 1, pp. 1–10, Jun. 2020.

[22] C. Lu and J. Yuan, "Adaptive super-twisting sliding mode control of permanent magnet synchronous motor," *Complexity*, vol. 2021, pp. 1–9, Aug. 2021.
[23] M. S. Zaky, M. K. Metwaly, H. Z. Azazi, and S. A. Deraz, "A new adaptive SMO for speed estimation of sensorless induction motor drives at zero and very low frequencies," *IEEE Trans. Ind. Electron.*, vol. 65, no. 9, pp. 6901–6911, Sep. 2018.
[24] D. Liang, J. Li, and R. Qu, "Super-twisting algorithm based sliding-mode observer with online parameter estimation for sensorless control of permanent magnet synchronous machine," in *Proc. IEEE Energy Convers. Congr. Expo. (ECCE)*, Milwaukee, WI, USA, 2016, pp. 1–8.
[25] G. Bartolini, E. Punta, and T. Zolezzi, "Regular simplex method and chattering elimination for nonlinear sliding mode control of uncertain systems," in *Proc. 46th IEEE Conf. Decis. Control*, New Orleans, LA, USA, 2007, pp. 2029–2034.
[26] J. Yang, M. Dou, and D. Zhao, "Iterative sliding mode observer for sensorless control of five-phase permanent magnet synchronous motor," *Bull. Polish Acad. Sci. Tech. Sci.*, vol. 65, no. 6, pp. 845–857, Dec. 2017.
[27] C. Lascu and F. Blaabjerg, "Super-twisting sliding mode direct torque contol of induction machine drives," in *Proc. IEEE Energy Convers. Congr. Expo. (ECCE)*, Pittsburgh, PA, USA, Sep. 2014, pp. 5116–5122.
[28] T. Gonzalez, J. A. Moreno, and L. Fridman, "Variable gain super-twisting sliding mode control," *IEEE Trans. Autom. Control*, vol. 57, no. 8, pp. 2100–2105, Aug. 2012.
[29] L. Kouriche and Y. Messlem, "MRAS-super twisting sliding mode observer for speed sensorless vector control of induction motor drive," *Przeglad Elektrotechniczny*, vol. 97, no. 4, pp. 121–127, Apr. 2021.
[30] D. Biel, E. Fossas, C. Meza, and R. Munoz, "Robust exact differentiation via sliding mode technique applied to a fixed-frequency quasi-sliding control algorithm," *ACES-Control Avancat De Sistemes D'energia*, vol. 75, pp. 1–13, Jan. 2008.
[31] L. Wogi, T. Ayana, M. Morawiec, and A. Jąderko, "A comparative study of fuzzy SMC with adaptive fuzzy PID for sensorless speed control of six-phase induction motor," *Energies*, vol. 15, no. 21, p. 8183, Nov. 2022.
[32] V. Kousalya and B. Singh, "Sensorless control of induction motor using MSTOGI based super twisting sliding mode flux observer for electric vehicle," in *Proc. IEEE Global Conf. Comput., Power Commun. Technol. (GlobConPT)*, New Delhi, India, Sep. 2022, pp. 1–6.
[33] A. Chalanga, S. Kamal, L. M. Fridman, B. Bandyopadhyay, and J. A. Moreno, "Implementation of super-twisting control: Super-twisting and higher order sliding-mode observer-based approaches," *IEEE Trans. Ind. Electron.*, vol. 63, no. 6, pp. 3677–3685, Jun. 2016.
[34] T. Wang, B. Wang, Y. Yu, and D. Xu, "High-order sliding-mode observer with adaptive gain for sensorless induction motor drives in the wide-speed range," *IEEE Trans. Ind. Electron.*, vol. 70, no. 11, pp. 11055–11066, Nov. 2023.
[35] M. Morawiec, P. Kroplewski, and C. Odeh, "Nonadaptive rotor speed estimation of induction machine in an adaptive full-order observer," *IEEE Trans. Ind. Electron.*, vol. 69, no. 3, pp. 2333–2344, Mar. 2022.
[36] Z. Krzeminski, "Nonlinear control of induction machines," in *Proc. 10th IFSC World Congr.*, Jul. 1987, pp. 349–354.
[37] T. Ayana, M. Morawiec, and L. Wogi, "Multiscalar control based airgap flux optimization of induction motor for loss minimization," *IEEE Access*, vol. 12, pp. 19993–20002, 2024.
[38] T. Ayana, L. Wogi, and M. Morawiec, "Core loss resistance impact on sensorless speed control of an induction motor using hybrid adaptive sliding mode observer," *Arch. Electr. Eng.*, vol. 72, no. 4, pp. 895–913, Dec. 2023.

LELISA WOGI received the B.Sc. degree in electrical and computer engineering from Jimma University, in 2017, and the M.Sc. degree in control and instrumentation engineering from Jimma Institute of Technology, Jimma, Ethiopia, in 2022. He is currently pursuing the Ph.D. degree with the Faculty of Electrical and Control Engineering, Department of Electric Drives and Energy Conversion, Gdańsk University of Technology, Gdańsk, Poland. Since 2017, he has been an Assistant Lecturer with Bule Hora University. He is the author of more than four articles. His research interests include nonlinear control of electrical machines, sensorless control, adaptive observer, and sliding mode control.

MARCIN MORAWIEC (Senior Member, IEEE) received the M.Sc. degree in electrical engineering from Czestochowa University of Technology, Poland, in 2003, the Ph.D. degree from Gdańsk University of Technology, Gdańsk, Poland, in 2007, and the D.Sc. degree in electrical drives, in 2017. He is currently a Professor with Gdańsk University of Technology. He is the author of more than 70 articles, two monographs and two chapters in books, one Polish patent, and five patent applications. His research interests include multiscalar models, nonlinear control of any electrical machine, sensorless control, nonlinear control, backstepping control, adaptive observer backstepping, and sliding mode control.

TADELE AYANA received the B.Sc. degree in electrical and computer engineering from Jimma University, in 2013, and the M.Sc. degree in control and instrumentation engineering from Jimma Institute of Technology, Jimma, Ethiopia, in 2018. He is currently pursuing the Ph.D. degree with the Faculty of Electrical and Control Engineering, Department of Electric Drives and Energy Conversion, Gdańsk University of Technology, Gdańsk, Poland. Since 2018, he has been a Lecturer with Jimma Institute of Technology. He is the author of more than six articles. His main research interests include multiscalar models, nonlinear control of electrical machines, sensorless control, nonlinear control, adaptive observer, and sliding mode control.